SZ effects in the Magneticum Pathfinder Simulation: Comparison with the Planck, SPT, and ACT results

K. Dolag^{1,2*}, E. Komatsu^{2,3} and R. Sunyaev^{2,4}

^{1} *University Observatory Munich, Scheinerstr. 1, 81679 Munich, Germany*
^{2} *Max-Planck-Institut für Astrophysik, Karl-Schwarzschild Strasse 1, 85748 Garching, Germany*
^{3} *Kavli Institute for the Physics and Mathematics of the Universe (Kavli IPMU, WPI), Todai Institutes for Advanced Study, the University of Tokyo, Kashiwa 277-8583, Japan*
^{4} *Space Research Institute (IKI), Russian Academy of Sciences, Profsoyuznaya str. 84/32, Moscow, 117997 Russia*

ABSTRACT

We calculate the one-point probability density distribution functions (PDF) and the power spectra of the thermal and kinetic Sunyaev-Zeldovich (tSZ and kSZ) effects and the mean Compton Y parameter using the *Magneticum Pathfinder* simulations, state-of-the-art cosmological hydrodynamical simulations of a large cosmological volume of $(896 \, \mathrm{Mpc}/h)^3$. These simulations follow in detail the thermal and chemical evolution of the intracluster medium as well as the evolution of super-massive black holes and their associated feedback processes. We construct full-sky maps of tSZ and kSZ from the light-cones out to $z = 0.17$, and one realisation of $8°.8 \times 8°.8$ deep light-cone out to $z = 5.2$. The local universe at $z < 0.027$ is simulated by a constrained realisation. The tail of the one-point PDF of tSZ from the deep light-cone follows a power-law shape with an index of -3.2. Once convolved with the effective beam of Planck, it agrees with the PDF measured by Planck. The predicted tSZ power spectrum agrees with that of the Planck data at all multipoles up to $l \approx 1000$, once the calculations are scaled to the Planck 2015 cosmological parameters with $\Omega_m = 0.308$ and $\sigma_8 = 0.8149$. Consistent with the results in the literature, however, we continue to find the tSZ power spectrum at $l = 3000$ that is significantly larger than that estimated from the high-resolution ground-based data. The simulation predicts the mean fluctuating Compton Y value of $\bar{Y} = 1.18 \times 10^{-6}$ for $\Omega_m = 0.272$ and $\sigma_8 = 0.809$. Nearly half ($\approx 5 \times 10^{-7}$) of the signal comes from halos below a virial mass of $10^{13} \, M_\odot/h$. Scaling this to the Planck 2015 parameters, we find $\bar{Y} = 1.57 \times 10^{-6}$. The PDF and the power spectrum of kSZ from our simulation agree broadly with the previous work.

Key words: hydrodynamics, method: numerical, galaxies: cluster: general, cosmic background radiation, cosmology: theory

1 INTRODUCTION

One of the last unsolved problems in cosmology with the cosmic microwave background (CMB) is connected with unknown levels of the spectral distortion of the black-body spectrum of CMB. Two decades ago the Far Infrared Absolute Spectrophotometer (FIRAS) on board NASA's Cosmic Background Explorer (COBE) provided the first limits (Fixsen et al. 1996) on the so-called y- and μ-type spectral distortions, which originate from energy releases in the present and early universe (Sunyaev & Zeldovich 1970b, 1980a). An enormous progress in technology of cryogenics and detectors of millimetre and sub-millimetre radiation enables us now to reach sensitivity which is 100 or even 1000 times better than that of FI-

RAS. A recently proposed PIXIE instrument is an example (Kogut et al. 2014).

While measuring the absolute monopole of the spectral distortions requires an absolute spectrometer such as FIRAS and PIXIE, the *fluctuating* component does not. Khatri & Sunyaev (2015) have recently demonstrated that the Planck data (Planck Collaboration et al. 2015c) permit to limit the mean of the fluctuating part of the y-type distortion to be $\bar{Y} < 2.2 \times 10^{-6}$ (where Y is the so-called Compton Y parameter), thereby reducing the observational upper bound by a factor of seven compared to the original COBE/FIRAS limit.[1]

The y-type spectral distortions do not carry information about

$\star$ E-mail: dolag@usm.uni-muenchen.de

---

[1] However, we should not forget that the COBE/FIRAS limit applies to the sum of the uniform and the fluctuating parts, whereas the Planck limit applies only to the latter.

redshifts at which they were produced. Therefore, it will be a challenge to distinguish between the primordial y-distortions originated from the pre-recombination era and those from a low-redshift universe induced by the large-scale structures. Nevertheless, in the standard thermal history of the universe, the latter component is expected to dominate by a couple of orders of magnitude[2]; namely, the dominant component of the mean Y is expected to come from the fluctuating component of the thermal Sunyaev-Zeldovich (tSZ) effect, i.e., inverse Compton scattering of low energy CMB photons on hot non-relativistic electrons in groups and clusters of galaxies (Sunyaev & Zeldovich 1970a). Therefore, the new Planck bound provides a limit on the total thermal energy content of hot gas in the universe. Indeed, this bound is approaching the predicted value of the mean Y calculated by the previous generations of cosmological hydrodynamical simulations; for example, Refregier et al. (2000) find $\bar{Y} = 1.67 \times 10^{-6}$ for a flat Λ Cold Dark Matter (CDM) model with $\Omega_m = 0.37$ and $\sigma_8 = 0.8$ (also see da Silva et al. 2000; Seljak et al. 2001; Zhang et al. 2004b). It is therefore timely to revisit this calculation with much improved, state-of-the-art simulations.

The Planck satellite has measured the power spectrum of fluctuations of tSZ on large angular scales ($l \lesssim 1000$). The tSZ power spectrum is very sensitive to the amplitude of matter density fluctuations (Komatsu & Kitayama 1999; Komatsu & Seljak 2002). The power spectrum on large angular scales is particularly a powerful probe of the amplitude of fluctuations, as it is less sensitive to astrophysics of the core of galaxy clusters than that at $l \approx 3000$ (Komatsu & Kitayama 1999; McCarthy et al. 2014).

Cosmological hydrodynamical simulations have proven essential in interpreting the observational data on the statistics of tSZ such as the power spectrum and the one-point probability density distribution function (PDF). The simulations have steadily improved over the past two decades, in terms of the numerical methods, the volume, the mass and spatial resolution, and implementation of baryonic physics such as cooling, heating, chemistry, and feedback processes (Persi et al. 1995; Refregier et al. 2000; da Silva et al. 2000; Seljak et al. 2001; Springel et al. 2001; da Silva et al. 2001b; Refregier & Teyssier 2002; White et al. 2002; Zhang et al. 2002; Dolag et al. 2005a; Roncarelli et al. 2007; Shaw et al. 2010; Battaglia et al. 2010, 2012; Munshi et al. 2013; McCarthy et al. 2014).

The recent progress in performing larger and more "complete" cosmological hydrodynamical simulations, which follow baryons in different phases such as in Warm-Hot Intergalactic Medium (WHIM,Cen & Ostriker (1999)), Intracluster Medium (ICM), stars and super massive black holes and their related feedback, allows now for a direct and detailed comparison of the predicted tSZ signals with observations. Such comparison may shed light on the recently reported tensions between cosmological parameters inferred from the primary CMB with the ones inferred from tSZ (Planck Collaboration et al. 2015c,b).

Scattering of CMB photons off electrons moving with a non-

zero line-of-sight bulk velocity with respect to the frame of coordinates where the CMB is isotropic yields temperature fluctuations by the Doppler shift of light, and this is known as the kinetic Sunyaev-Zeldovich (kSZ) effect (Sunyaev & Zeldovich 1970a, 1980b). There are two contributions to the kSZ signal: the reionisation contribution from $z \gtrsim 6$, and the post-reionisation contribution. The calculation of the former requires detailed reionisation simulations including radiative transfer and is beyond the scope of this paper. The calculation of the latter is in principle simpler than the former. Precisely characterising the post-reionisation kSZ is important, as we must subtract this contribution from the total kSZ to extract the reionisation contribution which, in turn, can constrain the physics of reionisation (see Zahn et al. 2012; Park et al. 2013, and references therein). Roughly speaking, the post-reionisation kSZ power spectrum is twice as large as that from reionisation; thus, ten per cent uncertainty in the post-reionisation contribution results in twenty per cent uncertainty in the reionisation contribution (Park et al. 2015).

In a fully ionised universe, the kSZ effect is given by the line-of-sight integration of the radial momentum field, i.e., a large-scale velocity field modulated by a small-scale density fluctuations of electrons (see Park et al. 2015, and references therein). Therefore, the calculation of the post-reionisation kSZ requires a simulation whose box size is large enough to capture the long-wavelength velocity field, and the spatial resolution high enough to resolve non-linear structures of baryons responsible for scattering of CMB photons. The hydrodynamical simulations of the post-reionisation kSZ have also improved over the past decade (Springel et al. 2001; da Silva et al. 2001a,b; White et al. 2002; Zhang et al. 2002, 2004a; Roncarelli et al. 2007; Shaw et al. 2012; Dolag & Sunyaev 2013). The measurements of the post-reionisation kSZ are improving rapidly as well (Hand et al. 2012; Li et al. 2014).

In this paper, we shall push the simulation frontier on the investigation of tSZ and kSZ further. The paper is organized as follows. Section 2 reviews the simulation method and the light-cone generation. Section 3 shows detailed comparisons of the simulation results with the observational data on the Coma cluster, and the one-point PDF and power spectrum of tSZ. We also show the simulation predictions for kSZ toward Coma, and the one-point PDF and power spectrum of kSZ. In section 4, we study how the mean Compton Y signal builds up over cosmic time. We summarise our findings in section 5.

2 SIMULATIONS

We construct sky maps of tSZ and kSZ using two sets of simulations: the "local universe" simulation (Sec. 2.1) based on a constrained realisation of the local universe at $z < 0.027$, and the *Magneticum Pathfinder* simulation (Sec. 2.2). Combining these simulations, we construct full-sky maps of tSZ and kSZ out to $z = 0.17$, and one realisation of $8°.8 \times 8°.8$ deep light-cone out to $z = 5.2$.

Both simulations are based on the parallel cosmological Tree Particle-Mesh (PM) Smoothed-particle Hydrodynamics (SPH) code P-GADGET3 (Springel 2005). The code uses an entropy-conserving formulation of SPH (Springel & Hernquist 2002) and follows the gas using a low-viscosity SPH scheme to properly track turbulence (Dolag et al. 2005b). Based on Dolag et al. (2004), it also follows thermal conduction at 1/20th of the classical Spitzer value (Spitzer 1962). It also allows a treatment of radiative cooling, heating from a uniform time-dependent ultraviolet background, and star formation with the associated feedback processes.

---

[2] In principle, knowing the precise expectation for the low-redshift tSZ contribution would make it possible to estimate the detectable level of the primordial y-type distortions from the pre-recombination era. In the absence of primordial non-Gaussianity, we do not expect any angular dependence of the y-type signal before recombination. Therefore, characterizing the angular dependence of the fluctuating component of the y-signal from the large-scale structures might open a possibility to separate that contribution from the primordial monopole (via, e.g., cross-correlation of tSZ with other tracers of the large-scale structure). If successful, we can retrieve information on the energy release at redshifts of $1000 \lesssim z \lesssim 20000$.

Radiative cooling rates are computed by following the same procedure presented by Wiersma et al. (2009). We account for the presence of the CMB and the ultraviolet (UV)/X-ray background radiation from quasars and galaxies, as computed by Haardt & Madau (2001). The contributions to cooling from each one of 11 elements (H, He, C, N, O, Ne, Mg, Si, S, Ca, Fe) have been pre-computed using the publicly available CLOUDY photo-ionization code (Ferland et al. 1998) for an optically thin gas in (photo-)ionization equilibrium.

We model the interstellar medium (ISM) by using a sub-resolution model for the multiphase ISM of Springel & Hernquist (2003). In this model, the ISM is treated as a two-phase medium, in which clouds of cold gas form by cooling of hot gas, and are embedded in the hot gas phase assuming pressure equilibrium whenever gas particles are above a given threshold density. The hot gas within the multiphase model is heated by supernovae and can evaporate the cold clouds. A certain fraction of massive stars (10 per cent) is assumed to explode as supernovae type II (SNII). The released energy by SNII (10^{51} erg) triggers galactic winds with a mass loading rate proportional to the star formation rate (SFR) with a resulting wind velocity of $v_{\rm wind} = 350$ km/s.

We include a detailed model of chemical evolution according to Tornatore et al. (2007). Metals are produced by SNII, by supernovae type Ia (SNIa) and by intermediate and low-mass stars in the asymptotic giant branch (AGB). Metals and energy are released by stars of different masses, by properly accounting for mass-dependent life-times (with a lifetime function according to Padovani & Matteucci 1993), the metallicity-dependent stellar yields by Woosley & Weaver (1995) for SNII, the yields by van den Hoek & Groenewegen (1997) for AGB stars, and the yields by Thielemann et al. (2003) for SNIa. Stars of different masses are initially distributed according to a Chabrier initial mass function (IMF; Chabrier 2003).

Most importantly, our simulations include prescriptions for the growth of black holes and the feedback from active galactic nuclei (AGN) based on the model of Springel et al. (2005) and Di Matteo et al. (2005) with the same modifications as in Fabjan et al. (2010) and some new, minor changes as described below.

The accretion onto black holes and the associated feedback adopts a sub-resolution model. Black holes are represented by collisionless "sink particles", which can grow in mass by either accreting gas from their environments, or merging with other black holes. The gas accretion rate, $\dot{M}_\bullet$, is estimated by the Bondi-Hoyle-Lyttleton approximation (Hoyle & Lyttleton 1939; Bondi & Hoyle 1944; Bondi 1952):

$$\dot{M}_\bullet = \frac{4\pi G^2 M_\bullet^2 f_{\rm boost} \rho}{(c_s^2 + v^2)^{3/2}}, \qquad (1)$$

where ρ and c_s are the density and the sound speed of the surrounding (ISM) gas, respectively, $f_{\rm boost}$ is a boost factor for the density which typically is set to 100 and v is the velocity of the black hole relative to the surrounding gas. The black hole accretion is always limited to the Eddington rate, i.e., the maximum possible accretion for balance between inwards-directed gravitational force and outwards-directed radiation pressure: $\dot{M}_\bullet = \min(\dot{M}_\bullet, \dot{M}_{\rm edd})$. Since the detailed accretion flows onto the black holes are unresolved, we can only capture black hole growth due to the larger scale, resolved gas distribution.

Once the accretion rate is computed for each BH particle, the mass continuously grows. To model the loss of this gas from the gas particles, a stochastic criterion is used to select the surrounding gas particles that are accreted. Unlike in Springel et al. (2005),

in which a selected gas particle contributes to accretion with all its mass, we include the possibility for a gas particle to accrete only with a fraction (1/4) of its original mass. In this way, each gas particle can contribute with up to four 'generations' of BH accretion events, thus providing a more continuous description of the accretion process.

As for the feedback, the radiated luminosity, $L_{\rm r}$, is related to the black hole accretion rate by

$$L_{\rm r} = \epsilon_{\rm r} \dot{M}_\bullet c^2, \qquad (2)$$

where $\epsilon_{\rm r}$ is the radiative efficiency, for which we adopt a fixed value of 0.1. This value is assumed typically for a radiatively efficient accretion disk onto a non-rapidly spinning black hole (Shakura & Sunyaev 1973; Springel 2005; Di Matteo et al. 2005). We assume that a fraction $\epsilon_{\rm f}$ of the radiated energy is thermally coupled to the surrounding gas; thus, $\dot{E}_{\rm f} = \epsilon_{\rm r} \epsilon_{\rm f} \dot{M}_\bullet c^2$ is the rate of the energy feedback. $\epsilon_{\rm f}$ is a free parameter and typically set to 0.1. The energy is distributed to the surrounding gas particles with weights similar to SPH. In addition, we incorporate the feedback prescription of Fabjan et al. (2010); namely, we account for a transition from a quasar- to a radio-mode feedback (see also Sijacki et al. 2007) whenever the accretion rate falls below an Eddington-ratio of $f_{\rm edd} \equiv \dot{M}_\bullet/\dot{M}_{\rm edd} < 10^{-2}$. During the radio-mode feedback we assume a 4 times larger feedback efficiency than in the quasar mode. This way, we attempt to account for massive black holes that are radiatively inefficient (having low accretion rates) but are efficient in heating the ICM by inflating hot bubbles in correspondence of the termination of AGN jets. In contrast to Springel et al. (2005), we modify the mass growth of the BH by taking into account the feedback, e.g., $\Delta M_\bullet = (1 - \epsilon_r)\dot{M}_\bullet \Delta t$. We introduced some more technical modifications of the original implementation, for which readers can find details in Hirschmann et al. (2014), where we also demonstrate that the bulk properties of the AGN population within the simulation are quite similar to the observed AGN properties.

2.1 Local Universe Simulation

The local universe simulation uses the final output of a cosmological hydrodynamical simulation of a constrained realisation of the local universe based on the nearly full-sky IRAS 1.2-Jy galaxy survey data (Fisher et al. 1994, 1995). The initial conditions are similar to those adopted by Mathis et al. (2002) in their study of structure formation in the local universe. The galaxy distribution in the IRAS 1.2-Jy galaxy survey is first smoothed by a Gaussian with a width of 7 Mpc and then linearly evolved back in time up to $z = 50$ following the method of Kolatt et al. (1996). The resulting field is then used as a constraint on phases of random Gaussian fields (Hoffman & Ribak 1991) for initialising the simulation.

The volume constrained by the observational data covers a sphere of radius ≈ 80 Mpc/h centered on the Milky Way. This region is sampled with more than 50 million high-resolution dark matter particles and is embedded in a periodic box of ≈ 240 Mpc/h on a side. The region outside the constrained volume is filled with nearly 7 million low-resolution dark matter particles, allowing a good coverage of long-range gravitational tidal forces. The gravitational force resolution (i.e., the softening length) of the simulation has been fixed to be 7 kpc/h (Plummer-equivalent), fixed in physical units from $z = 0$ to $z = 2$ and then stays constant in the corresponding co-moving units (e.g. 21 kpc/h) at higher redshifts.

Unlike in the original simulation made by Mathis et al. (2002), where only the dark matter component is present, here we follow
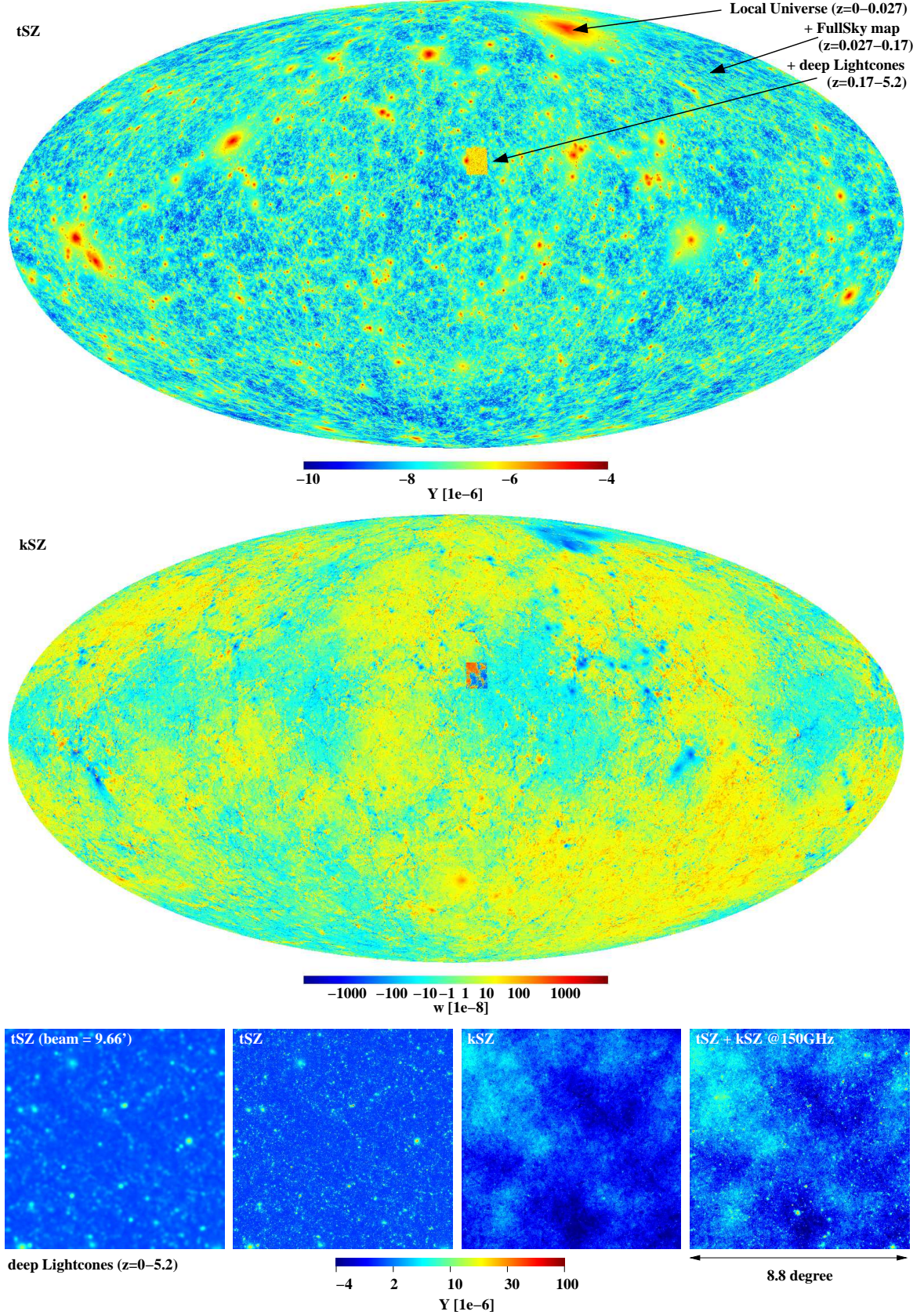
Figure 1. Full-sky maps of the Compton Y parameter (Eq. 3; top) and the kSZ effect (Eq. 4; middle) obtained from the local universe simulation ($z < 0.027$) combined with the full sky maps of the Magneticum Pathfinder simulation ($0.027 < z < 0.17$). We also show $8°.8 \times 8°.8$ maps from the deep light-cone of the Magneticum Pathfinder simulation restricted to $0.17 < z < 5.2$. The lower panels show, from the left to right: the Compton Y from the deep light-cone ($0 < z < 5.2$) smoothed with a 9.66 arcmin FWHM Gaussian beam; the Compton Y at the native resolution of HEALPix with nside=2048; the kSZ at the native resolution, and the sum of the two at 150 GHz (Eq. 5).
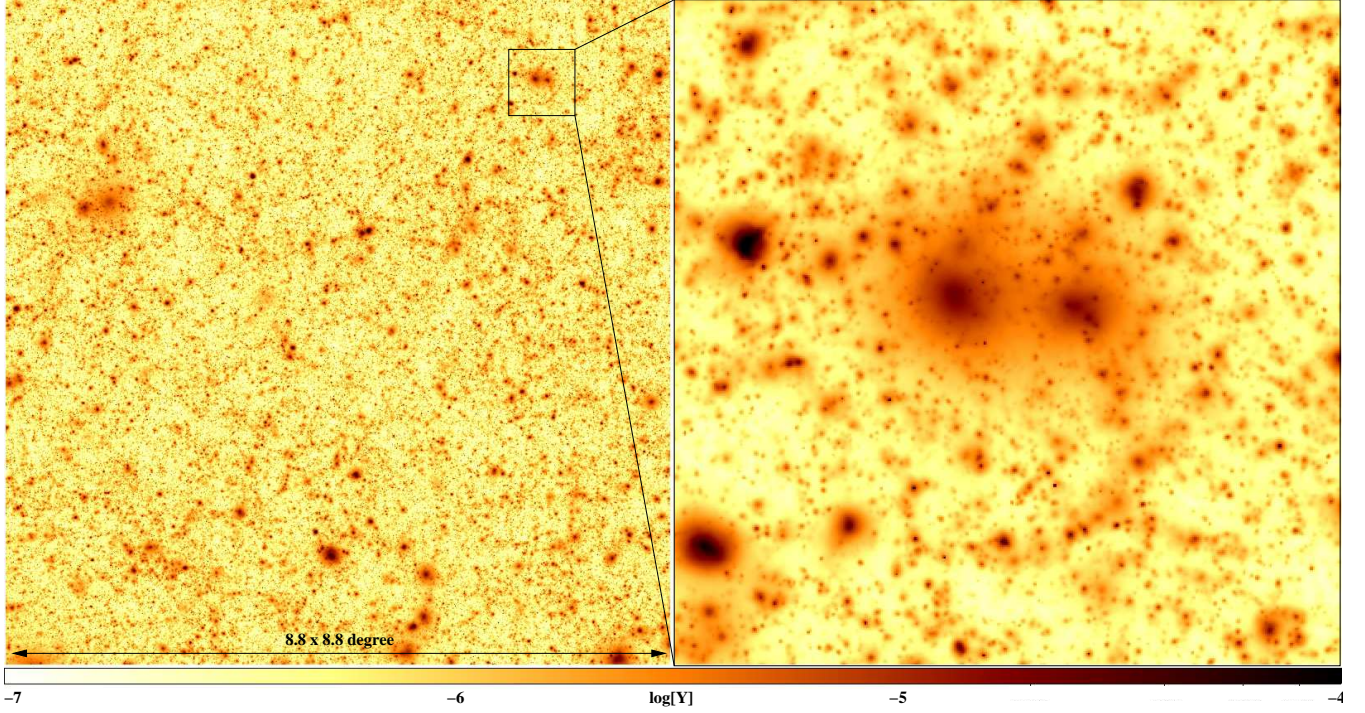
Figure 2. Compton Y from the deep light-cone ($0 < z < 5.2$). The right panel shows a zoom onto a region containing several rich clusters at various redshifts.

also the gas and stellar components. Therefore, we extend the initial conditions by splitting the original high-resolution dark matter particles into gas and dark matter particles having masses of $m_{gas} \approx 0.48 \times 10^9 \ M_\odot/h$ and $m_{dm} \approx 3.1 \times 10^9 \ M_\odot/h$, respectively; this corresponds to a cosmological baryon fraction of 13 per cent. The total number of particles within the simulation is slightly more than 108 million, and the most massive cluster is resolved by almost one million particles.

In this simulation, we assume a flat ΛCDM model with a present matter density parameter of $\Omega_m = 0.3$, a Hubble constant of $H_0 = 100 \ h$ km/s/Mpc with $h = 0.7$, and an r.m.s. density fluctuation of $\sigma_8 = 0.9$.

2.2 Magneticum Pathfinder Simulation

The *Magneticum Pathfinder*[3] simulation follows a large $(896 \ \text{Mpc}/h)^3$ box simulated using 2×1526^3 particles and adapting a WMAP7 (Komatsu et al. 2011) flat ΛCDM cosmology with $\sigma_8 = 0.809$, $h = 0.704$, $\Omega_m = 0.272$, $\Omega_b = 0.0456$, and an initial slope for the power spectrum of $n_s = 0.963$. Dark matter particles have a mass of $m_{DM} = 1.3 \times 10^{10} \ M_\odot/h$, gas particles have $m_{gas} \approx 2.6 \times 10^9 \ M_\odot/h$ depending on their enrichment history, and stellar particles have $m_{stars} \approx 7.5 \times 10^8 \ M_\odot/h$ depending on the state of the underlying stellar population. For gas and dark matter, the gravitational softening length is set to $10 \ \text{kpc}/h$ (Plummer-equivalent), fixed in physical units from $z = 0$ to $z = 2$ and then stays constant in the corresponding co-moving units (e.g. $30 \ \text{kpc}/h$) at higher redshifts. For star particles it is accordingly half the values (e.g. $5 \ \text{kpc}/h$ at $z = 0$). In this simulation, one gas particle can form up to four stellar particles.

[3] www.magneticum.org

2.3 Map Making

We construct maps from the simulations using SMAC (Dolag et al. 2005a), integrating both the tSZ and kSZ signals through our hydrodynamical simulations.

The tSZ signal in each pixel at a sky position θ is characterised by the Compton Y parameter defined by (Sunyaev & Zeldovich 1972)

$$Y_{\text{tSZ}}(\boldsymbol{\theta}) = \frac{k_B \sigma_T}{m_e c^2} \int \text{d}l \ n_e(\boldsymbol{\theta}, l) \ T(\boldsymbol{\theta}, l) \ , \tag{3}$$

where n_e and T are the three-dimensional number density and temperature of thermal electrons, respectively, and k_B, σ_T, m_e, and c are the Boltzmann constant, the Thomson scattering cross section, the electron mass, and the speed of light, respectively. The kSZ signal is obtained by (Sunyaev & Zeldovich 1970a, 1980b)

$$w_{\text{kSZ}}(\boldsymbol{\theta}) \equiv \frac{\delta T_{\text{kSZ}}}{T_{\text{cmb}}} = -\frac{\sigma_T}{c} \int \text{d}l \ n_e(\boldsymbol{\theta}, l) \ v_r(\boldsymbol{\theta}, l) \ , \tag{4}$$

where $T_{\text{cmb}} = 2.725$ K and v_r is the radial component of the peculiar bulk velocity, defined such that $v_r > 0$ for gas moving away from us.

As the tSZ and kSZ have different dependence on the observed frequencies, we use the following weighted sum of the two when showing the combined signal:

$$Y_{\text{eff}}^{\text{frq}} \equiv \frac{g(x) Y_{\text{tSZ}} - w_{\text{kSZ}}}{g(x)} \ , \tag{5}$$

with

$$g(x) = \frac{x(e^x + 1)}{(e^x - 1)} - 4 \ , \tag{6}$$

derived by Zeldovich & Sunyaev (1969), where $x = \text{frq}[GHz]/56.8$. The temperature anisotropy due to tSZ is given by $\delta T_{\text{tSZ}}/T_{\text{cmb}} = g(x)Y$, where we ignore relativistic corrections.
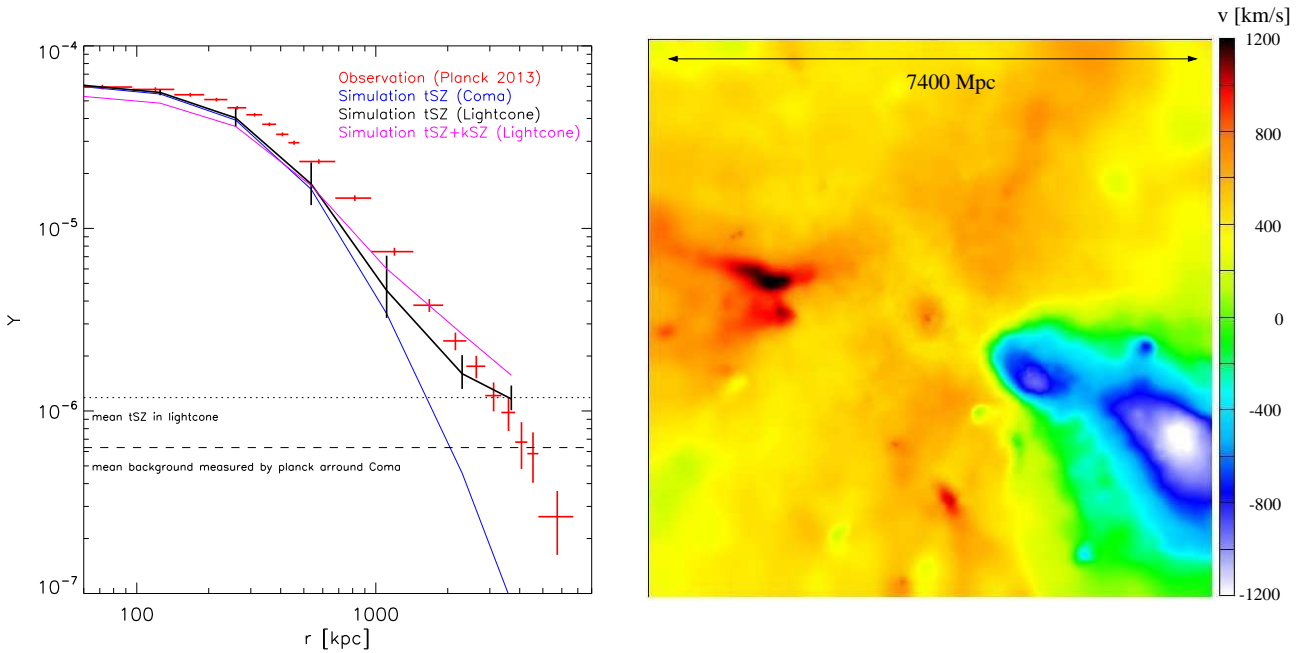
Figure 3. Compton Y profile of the Coma cluster (left panel). The symbols show the Planck data taken from Planck Collaboration et al. (2013c). These data points have an estimate of the mean background (horizontal dashed line) subtracted by the Planck team. The blue line shows the Compton Y toward the counterpart of the Coma cluster in the local universe simulation, while the thick black solid line shows the Coma cluster embedded in the deep light-cone of the Magneticum Pathfinder simulation, to show the effect of the contribution of gas outside the Coma cluster. All simulated maps are smoothed with a Gaussian beam of 10 arcmin. The error bars on the thick black solid line show the 25% and 75% percentile of the Compton Y distribution in each radial bin, averaged over 9 different maps obtained by placing Coma at different positions within the light-cone. The horizontal dotted line shows the mean Compton Y of the deep light-cone, $\bar{Y} = 1.18 \times 10^{-6}$. The magenta line shows the sum of tSZ and kSZ (Eq. 5) at 150 GHz. In the local universe simulation, Coma is moving away from us, thus giving a negative kSZ near the center. On the other hand, a positive kSZ in the outskirt is due to a massive, gas rich sub-structure moving toward us, as shown in the mass-weighted velocity map of Coma in the local universe simulation (right panel).

We produced full-sky maps of the Compton Y and kSZ in the HEALPix (Górski et al. 1998) format with Nside=2048 from the local universe ($0 < z < 0.027$) and from the Magneticum Pathfinder simulation covering $0.027 < z < 0.17$. We also produced a realization of one deep, $8°.8 \times 8°.8$ light-cone covering $0 < z < 5.2$. When we combine the deep light-cone with the full-sky maps, we use only the relevant parts, $0.027 < z < 5.2$ or $0.17 < z < 5.2$, of the deep light-cone.

In figure 1, we show the full-sky maps of the Compton Y (top panel) and kSZ (middle) where the local universe simulation is combined with the Magneticum Pathfinder simulation. We also show $0.17 < z < 5.2$ of the of deep light-cone (as indicated by the arrow) to give the impression of the additional SZ signals covered by the deep light-cone. The lower panels show the Compton Y from the deep light-cone ($0 < z < 5.2$) smoothed with a 9.66 arcmin FWHM Gaussian beam as well as the native resolution and the same with the kSZ signal added at 150 GHz (Eq. 5). The deep light-cone contains about 8000 galaxy clusters and groups with virial masses above $10^{13.5} \, M_\odot/h$, contributing to the most prominent structures visible in the zoom onto a sub-part of the Compton Y map shown in the right panel of figure 2.

3   COMPARISON WITH THE PLANCK DATA

3.1   Coma

The thermal electron pressure determines the (non-relativistic) tSZ effect. Azimuthally-averaged radial profiles of thermal pressure in galaxy clusters identified in our hydrodynamical simulations follow the so-called "universe pressure profile" (Arnaud et al. 2010a). The stacked pressure profiles of galaxy-cluster-size halos in our simulation are in good agreement with the stacked pressure profiles inferred from the tSZ data on galaxy clusters detected by Planck (Planck Collaboration et al. 2013a) and South Pole Telescope (SPT) (McDonald et al. 2014). However, such comparisons allows only a statistical comparison of the averaged profiles.

Local, well-resolved galaxy clusters enable a more detailed object-by-object comparison. Here we make use of the fact that the constrained simulation of the local universe allows to cross-identify objects in the simulations with the real-world counterparts. Despite the relatively low spacial resolution (e.g., > 5 Mpc) of the constraints used for initialising the simulation (see Mathis et al. 2002, for details), local galaxy clusters like the Coma cluster have a remarkably similar counterpart in the simulation.

In the left panel of figure 3, we compare the radial profiles of tSZ (the Compton Y parameter given in Eq. 3), as well as the significant contribution of kSZ at 150 GHz (as given in Eqs. 4 and 5), toward the Coma cluster in the simulation with the Planck tSZ data for Coma (Planck Collaboration et al. 2013c). The blue line shows the Compton Y toward the "Coma cluster" in the local universe simulation out to a co-moving distance of 110 Mpc, while the thick black solid line shows the "Coma cluster" embedded in the deep light-cone out to $z = 5.2$. The latter has more signal in the outskirt of the cluster because of the contributions from hot gas outside Coma.
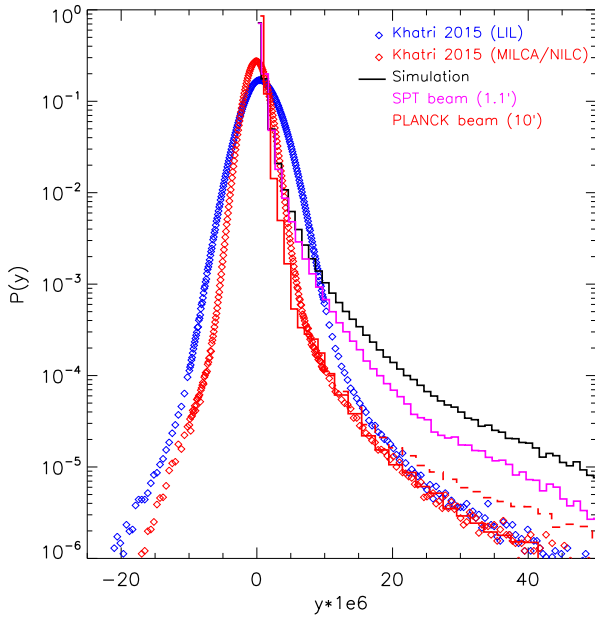
We find an excellent agreement between the simulation and

Figure 4. PDFs of the Compton Y parameter, normalised such that $\int dy\, P(y) = 1$. The black line shows the PDF of the deep $8°.8 \times 8°.8$ light-cone out to $z = 5.2$ without any smoothing applied, while the magenta line shows the PDF smoothed with 1.1 arcmin FWHM beam to simulate the signal that would be measured by SPT. The red and blue symbols show the measurements from the Planck data using different methods (Khatri & Sunyaev 2015; Khatri 2015). The blue method yields larger noise in the Compton Y map, and thus has a broader core in the middle, while both methods agree well in the tail. The dashed red line shows the PDF of the local universe simulation, smoothed with 10 arcmin FWHM beam to simulate the Planck data. The excess at large Y values above the Planck data is due to the structures like Perseus-Pisces that are masked when the measurement is done. Applying the same mask with $f_{\rm sky} = 0.51$ as used by Khatri & Sunyaev (2015), we find that the PDF from the simulation agrees with the Planck data in the tail (solid red line). In the core, our PDF is narrower than the Planck data, as our PDF does not include instrumental noise. Note that the PDF of the deep light-cone is also included in the red solid line, whose contribution dominates in the core.

the Planck data (shown as the symbols) in the inner part, $r \lesssim 100$ kpc. The full light-cone integration (thick black line) agrees reasonably well with the Planck data up to a few Mpc. Given the uncertainties in the constrained simulation, this level of agreement is remarkable. Also the mean Compton Y ($\bar{Y} = 1.18 \times 10^{-6}$), obtained from the deep light-cone (shown by the horizontal dotted line) agrees with the background subtracted from the Planck data (shown by the horizontal dashed line) to within a factor of two.

Finally, to get a feel for the magnitude of kSZ toward the "Coma cluster", we show the sum of tSZ and kSZ at 150 GHz (Eq. 5) in the magenta line. Both include the full light-cone integration out to $z = 5.2$. For this particular realisation, we find a non-negligible (10 to 20 per cent) contribution from kSZ.[4] In particular, we find that the local universe simulation predicts that the overall halo of Coma is moving away from us at ≈ 400 km/s with

respect to the CMB rest frame, yielding a negative kSZ signal up to Mpc radius. Being a merging system, the core of Coma in our realisation moves with even higher velocity (up to 800 km/s) as commonly seen in simulations (ZuHone et al. 2010; Dolag & Sunyaev 2013) near the center.

We also find a large, positive kSZ signal in the outskirt, which is due to a massive, gas-rich infalling sub-structure moving toward us. See the right panel of figure 3 for a map of the mass-weighted velocity field around Coma. While the overall halo velocity predicted for Coma should be accurate to the extent of the precision of the constraints used by the local universe simulation, details of sub-structures present in this realization of the local universe are far outside the predictive power of such a simulation. Therefore, the prediction for a positive kSZ in the outskirt and the phase of movement of the core should be interpreted with caution.

3.2 The Compton Y Map

In figure 4, we compare the one-point PDF of the Compton Y map from the simulations (lines) with that observed by Planck (symbols; Planck Collaboration et al. 2014b; Khatri & Sunyaev 2015; Khatri 2015). The asymmetry of the left and right tails (skewness) of $P(y)$ is due to galaxy clusters and groups along the lines of sight, as predicted previously (Yoshida et al. 2001; Rubiño-Martín & Sunyaev 2003). In the absence of noise, the pixel values in the simulations are always positive, whereas Planck's Y values can have negative values due to noise (or unaccounted other sources).

As our maps have significantly higher spatial resolution than Planck, we find a larger excess of high Y values (black line), driven by the central parts of halos along the lines of sight. This can be best seen in figure 2, especially in the zoom-in in the right panel. However, once smoothed with the beam size of Planck's Y map (10 arcmin FWHM), the excess due to these structures unresolved by Planck is reduced (red dashed line), and the simulation and the Planck data are in much better agreement up to $Y \approx 2 \times 10^{-5}$. The effect of the beam smearing in the light-cone map can be seen visually in the left most panel in the bottom panels of figure 1. With the smoothing size as large as this, the excess PDF at larger values of Y above the Planck data is dominated by the nearby structures that subtend large angles in the sky. We find that the excess is dominated by the structures in the local universe simulation. Remarkably, we could identify the source of the excess PDF as the structures such as Perseus-Pisces that are masked when the measurement is done. Using the same mask that retains 51% of the sky used by Khatri & Sunyaev (2015), we find an excellent agreement between the PDFs from the simulation (red solid line) and the Planck data at all values of Y. The "core" of the PDF from the simulation at small values of Y is dominated by the structures in the deep light-cone beyond the local universe simulation, and is narrower than the Planck data because the simulation does not include Planck's instrumental noise.

We also convolve our map with the SPT beam (1.1 arcmin FWHM; magenta line). In this case, the excess at large Compton Y values is only mildly suppressed, demonstrating that SPT-like instruments would be able to resolve almost all the contributions of structures resolved by our simulation. See Hill et al. (2014) for the measurement and interpretation of the one-point PDF of the ACT data.

Coming back to the unsmoothed PDF, we find that the tail of the PDF follows a power law shape over at least two orders of magnitude in Compton Y values. The slope of this power law is approximately -3.2 as shown by the dashed line in the left panel of figure 5.

---

[4] However, we should not compare the magenta line with the Planck data in the left panel of figure 3, as the Planck data shown here are obtained by combining the multi-frequency Planck data specifically to extract tSZ, and most (if not all) of kSZ has been removed.

The middle panel shows the PDF of kSZ. It shows a non-Gaussian tail in agreement with the previous work (da Silva et al. 2001a; Yoshida et al. 2001). The right panel shows the PDF of the sum of tSZ and kSZ (Y_{eff} defined in Eq. 5) at various Planck frequencies. The contribution to the PDF of Y_{eff} of the kSZ signal is negligible for $Y_{\text{eff}} \gtrsim 10^{-5}$, while it significantly modifies the PDF at smaller values of Y_{eff}. As the PDF of kSZ is flatter at small values of kSZ than that of the Compton Y at small values of Y, the PDF of the sum of the two shows an excess probability in $10^{-6} \lesssim Y_{\text{eff}} \lesssim 10^{-5}$ (see the solid lines figure 5). The dashed lines show the PDF for negative values of Y_{eff}. This unique shape of the PDF, which changes as a function of frequencies in a predictable way, may be used to detect the kSZ signals in the data.

3.3 The angular power spectra of tSZ and kSZ

3.3.1 Simulation results

To calculate the angular power spectrum of tSZ, we separately use the full-sky map obtained from the local universe simulation in $z < 0.027$ and the light-cones over $8°.8 \times 8°.8$ in $0.027 < z < 5.2$. As these simulations are performed with different cosmological parameters, we rescale the amplitudes of the tSZ power spectra by $\sigma_8^8 \Omega_m^3$ to Planck 2015's best fitting CMB cosmological values, $\Omega_m = 0.308$ and $\sigma_8 = 0.8149$ ("TT+lowP+lensing" of Planck Collaboration et al. 2015a). We have checked that this scaling agrees with the scaling predicted by the analytical calculation presented in section 3.3.2

Figure 6 shows the tSZ power spectrum measured by Planck at 150 GHz (red symbols with error bars; Planck Collaboration et al. 2015c). Two dashed lines show the tSZ power spectrum from the local universe at low multipoles and that from the light-cone at high multipoles, while the black solid line shows the sum of the two. This division in multipoles is consistent with the previous work showing that the nearby structures dominate at low multipoles simply because they appear larger in the sky (Refregier et al. 2000; Komatsu & Seljak 2002; Dolag et al. 2005a; Hansen et al. 2005).

The black solid line agrees with the Planck data well at all multipoles measured by Planck, i.e., $l \lesssim 1000$. Our conclusion that the predicted tSZ power spectrum with Planck 2015's TT+lowP+lensing parameters agrees with the measured power spectrum is consistent with the finding of the Planck team (Planck Collaboration et al. 2015c). McCarthy et al. (2014) show that the Planck 2013 parameters with $\Omega_m = 0.3175$ and $\sigma_8 = 0.834$ (Planck Collaboration et al. 2014a) over-predict the tSZ power spectrum, and show that another set of parameters with $\Omega_m = 0.302$ and $\sigma_8 = 0.817$ (Spergel et al. 2015) gives the tSZ power spectrum in agreement with the measurement. The latter set is close to the Planck 2015 parameters with lensing that we use in this paper; thus, our conclusion is consistent with their results. Using the $\Omega_m^3 \sigma_8^8$ scaling, for example, the former set gives 32% larger power than the 2015 parameters, while the latter gives 4% smaller power.

However, at $l \approx 3000$, our prediction is significantly higher than the measurements reported by SPT and Atacama Cosmology Telescope (ACT) collaborations (Reichardt et al. 2012; Sievers et al. 2013). This finding is not new: the previous calculations of the tSZ power spectrum also over-predict the power at $l \approx 3000$ compared to the SPT and ACT data, although the degree of over-estimation varies depending on the details of baryonic physics implemented in the models (e.g., McCarthy et al. 2014; George et al. 2015; Ramos-Ceja et al. 2014).

Whether this discrepancy at $l \approx 3000$ poses a serious challenge to theory is unclear, given that the SPT and ACT do not have as many frequency channels as Planck. Distinguishing the primary CMB, tSZ, and the other extra-galactic sources by their frequency dependence is more challenging for SPT and ACT. (On the other hand, Planck does not have angular resolution to resolve the power at $l \approx 3000$.) The tSZ signal is a sub-dominant contribution to the power spectrum at $l \approx 3000$ compared to the extra-galactic sources. The magenta symbols with error bars in figure 6 show the SPT power spectrum with the best-fitting primary CMB power spectrum subtracted. The difference between the magenta symbols and a magenta vertical line at $l = 3000$ indicates the amount of the extra-galactic power that needs to be subtracted. At least, our tSZ power spectrum does not overshoot the magenta data points that provide a firm upper limit on the tSZ power at these angular scales.

Next, we show the kSZ power spectrum from the light-cones by the blue solid line in figure 6. Our result at high multipoles ($l \gtrsim 1000$) agrees with that of Shaw et al. (2012). The upturn at lower multipoles can be understood by the contribution from the longitudinal velocity contributions that did not fully cancel by the line-of-sight integration (Hernández-Monteagudo & Ho 2009). At 150 GHz, the kSZ amplitude becomes comparable to tSZ at $l \approx 300$, and becomes even dominant at lower multipoles. (Note that the Planck data shown in this figure remove most of the kSZ signals by construction, and thus should not be compared with the blue line.) However, as the kSZ signal is dominated by the largest modes present in the simulation (see figure 1), even larger cosmological volumes will be needed to obtain a fully converged kSZ results from such light-cones.

3.3.2 Analytical model of the tSZ power spectrum

To check accuracy of scaling the tSZ power spectrum to other cosmological parameters, we compute the tSZ power spectrum using an analytical model. Ignoring a small contribution from the correlation between two distinct dark matter halos (Komatsu & Kitayama 1999), we model the SZ power spectrum as (Komatsu & Seljak 2002)

$$C_l = g^2(x) \int_0^5 dz \frac{dV}{dz} \int_{M_{\text{min}}}^{M_{\text{max}}} d\ln M \frac{dn(M,z)}{d\ln M} |\tilde{y}_l(M,z)|^2 ,$$

(7)

where M is the virial mass with $(M_{\text{min}}, M_{\text{max}}) = (5 \times 10^{11} M_\odot, 5 \times 10^{15} M_\odot)$, dV/dz is the differential comoving volume per steradian, and $dn/d\ln M$ is the halo mass function given by

$$\frac{dn(M,z)}{d\ln M} = \frac{d\ln M_{\text{200m}}}{d\ln M} \frac{dn(M_{\text{200m}},z)}{d\ln M_{\text{200m}}} ,$$

(8)

with $dn/d\ln M_{\text{200m}}$ derived from simulations. Here, M_{200m} is the mass enclosed within r_{200m}, in which the mean overdensity is 200 times the mean mass density of the universe. We convert M to M_{200m} using an NFW profile (Navarro et al. 1996, 1997) with the concentration parameter of Duffy et al. (2008) (see, e.g., Eq. 14 of Komatsu & Seljak 2001). For the mass range we consider, we find $d\ln M_{\text{200m}}/d\ln M \approx 1$ to good approximation.

For $dn/d\ln M_{\text{200m}}$, we use three different sets of fit parameters obtained from numerical simulations in the literature. First, we use the mass function from the Magneticum Pathfinder simulation (Eq. 1 and 3 of Bocquet et al. 2015, with the parameters for "M_{200m} Hydro" given in their Table 2. Using "M_{200m} DMonly" gives a similar result: the difference in the power spectrum is less than four percent at all multipoles). This mass function should give
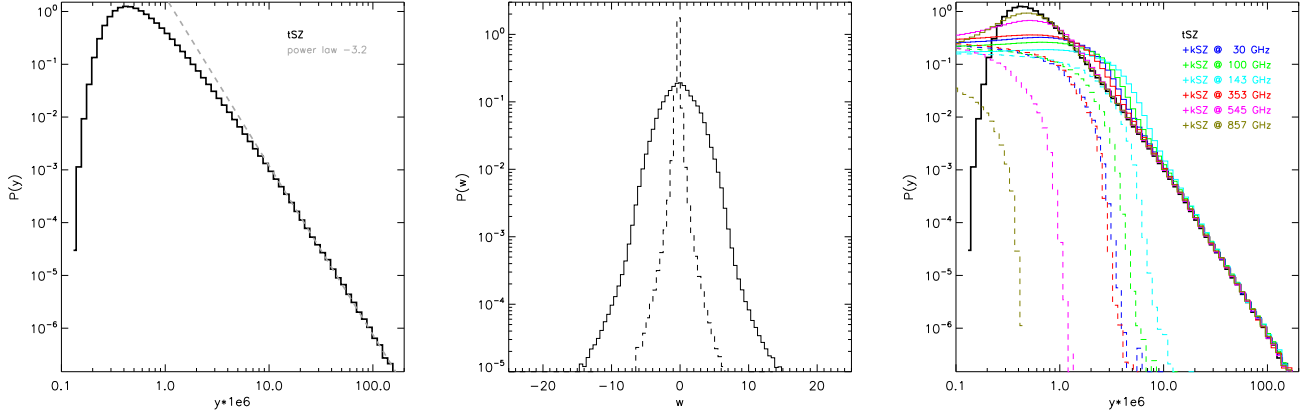
Figure 5. PDFs of the SZ effects computed from the deep light-cone. (Left) PDF of the Compton Y parameter, which is the same as the black line in figure 4, normalised such that $\int dY\, P(Y) = 1$. The dashed line shows a power-law with a slope of -3.2. (Middle) PDF of kSZ, normalised such that $\int dw\, P(w) = 1$. The dashed line shows the PDF at $z = 0$ (see Yoshida et al. 2001, for comparison), while the solid line shows the PDF from the light-cone. (Right) PDF of the sum of the two (Eq. 5) at various Planck frequencies, normalised such that $\int dY_{\rm eff}\, P(Y_{\rm eff}) = 1$. The solid lines show PDFs for $Y_{\rm eff} > 0$ while the dashed lines show those for $Y_{\rm eff} < 0$.

the result that is most consistent with the black solid line shown in figure 6. The other mass function fits are taken from Tinker et al. (2008) and Tinker et al. (2010).

To compute the linear r.m.s. mass density fluctuation necessary in the fitting formulae of the mass function, we use the CAMB code (Lewis et al. 2000) to generate the linear matter power spectrum with the Planck 2015 "TT+lowP+lensing" parameters: $\Omega_b h^2 = 0.02226$, $\Omega_c h^2 = 0.1186$, $\Omega_\nu h^2 = 0.00064$, $h = 0.6781$, $\Delta_\mathcal{R}^2(0.05\ {\rm Mpc}^{-1}) = 2.139 \times 10^{-9}$, and $n_s = 0.9677$ (Planck Collaboration et al. 2015a).

The 2D Fourier transform of the Compton Y parameter, $\tilde{y}_l$, is given by

$$\tilde{y}_l = \frac{4\pi r_{500}}{l_{500}^2}\frac{\sigma_T}{m_e c^2}\int_0^6 dx\, x^2 P_e(x)\frac{\sin(lx/l_{500})}{lx/l_{500}}\,, \qquad (9)$$

where $x = r/r_{500}$, $l_{500} \equiv D_A/r_{500}$, D_A is the proper angular diameter distance, and r_{500} is the radius within which the mean overdensity is 500 times the critical density of the universe. Again, we convert M to M_{500} using an NFW profile with the concentration parameter of Duffy et al. (2008). For the electron pressure profile, P_e, we use the following parametrized profile (Nagai et al. 2007; Arnaud et al. 2010b):

$$
\begin{aligned}
P_e(x) &= 1.65\,(h/0.7)^2\ {\rm eV\ cm}^{-3} \\
&\times\ E^{8/3}(z)\left[\frac{M_{500}}{3 \times 10^{14}(0.7/h)M_\odot}\right]^{2/3+\alpha_p} p(x),\ (10)
\end{aligned}
$$

with $\alpha_p = 0.12$, $E(z) \equiv H(z)/H_0 = \left[\Omega_m(1+z)^3 + 1 - \Omega_m\right]^{1/2}$, and the function $p(x)$ is defined by

$$p(x) \equiv \frac{6.41(0.7/h)^{3/2}}{(c_{500}x)^\gamma[1 + (c_{500}x)^\alpha]^{(\beta-\gamma)/\alpha}}, \qquad (11)$$

with $c_{500} = 1.81$, $\alpha = 1.33$, $\beta = 4.13$, and $\gamma = 0.31$ (Planck Collaboration et al. 2013b). However, this fitting function for the pressure profile was derived for M_{500} assuming hydrostatic equilibrium, which is known to be biased low relative to the true M_{500} due to non-thermal pressure (see, e.g., Shi & Komatsu 2014, and references therein). We thus rescale M_{500} in Eq. 10 as $M_{500} \rightarrow M_{500}/1.2$ and r_{500} (hence l_{500}) in Eq. 9 as $r_{500} \rightarrow r_{500}/1.2^{1/3}$ to account for the hydrostatic mass bias. This correction brings

the pressure profiles in the Magneticum Pathfinder simulation into good agreement with the Planck data (Planck Collaboration et al. 2013b).

The light blue solid line shows the analytical model calculation with the mass function of Bocquet et al. (2015), which is in good agreement with the results obtained directly from the simulation at $l \lesssim 1000$, while it under-predicts the power at higher multipoles. This can be understood partially as due to inhomogeneity in the distribution of pressure within halos, as the analytical model assumes a smooth distribution of pressure. Battaglia et al. (2012) show that inhomogeneity increases the power at these high multipoles by 20%. The remaining difference may be due to the pressure profile of low-mass halos (less than $10^{14}\ M_\odot$) in the Magneticum Simulation being slightly different from the Planck pressure profile given in Eq. 10, as well as to the normalisation of the mass function for low-mass halos (see the next paragraph). In any case, the overall agreement between the simulation and the analytical model is satisfactory.

The analytical models with the other mass functions yield similar, but different, results. The only difference between the mass functions of Tinker et al. (2008) and Tinker et al. (2010) is that the latter forces the normalisation of the mass function by $\int_0^\infty dM_{200m}\, dn/d\ln M_{200m} = \bar{\rho}$, where $\bar{\rho}$ is the mean mass density of the universe. This normalisation mainly changes the abundance of low-mass halos which are not well resolved by their N-body simulations. As a result, the latter mass function (shown as the dashed light blue line in figure 6) gives larger power at high multipoles where the contributions from low-mass halos dominate.

At $l \lesssim 100$, the tSZ power spectra with both Tinker et al. mass functions are slightly larger than that with the mass function of Bocquet et al. (2015) (20 and 15 per cent larger at $l = 10$ and 100, respectively). Indeed, the fitting formula for the mass function of Bocquet et al. (2015) gives similarly smaller $dn/d\ln M_{200m}$ than the fits of Tinker et al. mass functions at the relevant mass scales, i.e., $M_{200m} \gtrsim 10^{15}\ M_\odot$. Bocquet et al. (2015) explain this by the way the fits are performed; namely, the actual data of the N-body simulations are similar between Bocquet et al. and Tinker et al., but the fitting procedures give slightly different results. Bocquet et al. use the Bayesian likelihood approach taking into ac-
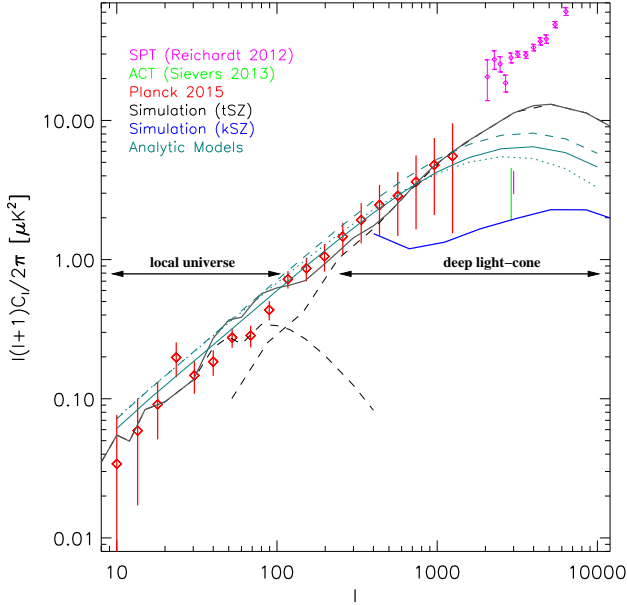
Figure 6. Power spectra of temperature anisotropies due to tSZ and kSZ at 150 GHz in units of μK^2. The red symbols with error bars show the estimation of the tSZ power spectrum from the Planck data (Planck Collaboration et al. 2015c), while the magenta symbols with error bars show the power spectrum of the SPT data (Reichardt et al. 2012) with the best-fitting primary CMB power spectrum subtracted. The green and magenta vertical lines show the ranges of the estimated tSZ power spectra at $l = 3000$ by ACT (Sievers et al. 2013) and SPT, respectively. The black dashed lines show the tSZ power spectrum of the full-sky, local universe simulation ($z < 0.027$) at low multipoles, and that of the deep, $8°.8 \times 8°.8$ light-cone from the Magneticum Pathfinder simulations ($0.027 < z < 5.2$) at high multipoles. The black solid line shows the sum of the two. Both power spectra are scaled to Planck 2015's "TT+lowP+lensing" cosmological parameters of $\Omega_m = 0.308$ and $\sigma_8 = 0.8149$. The light blue lines show the analytical predictions based on three different mass functions (see section 3.3.2). The solid blue line shows kSZ power spectrum of the deep light-cone.

count properly the Poisson nature of the mass function measured from the simulation, whereas Tinker et al. use the χ^2 statistics. The former results do not depend on the bin size of the mass in which the fits to $dn/d \ln M_{200m}$ are performed, whereas the latter results do. Our results highlight the importance of better understanding the high-mass end of the mass function for the study of the tSZ power spectrum.

4   MEAN COMPTON Y

4.1   Simulation results

The deep light-cone yields the mean Compton Y of $\bar{Y} = 1.18 \times 10^{-6}$ (shown as the dotted horizontal line in figure 3) for the cosmological parameters used in the Magneticum Pathfinder simulation: $\sigma_8 = 0.809$ and $\Omega_m = 0.272$. We now study how $\bar{Y}$ builds up over cosmic time and how much objects of different masses contribute to $\bar{Y}$. To this end, we proceed similar to the construction of the different slabs contributing to the light-cone. However, to avoid that the volume (and therefore the statistics) decreases with decreasing redshift like the volume swept by a light-cone of a given
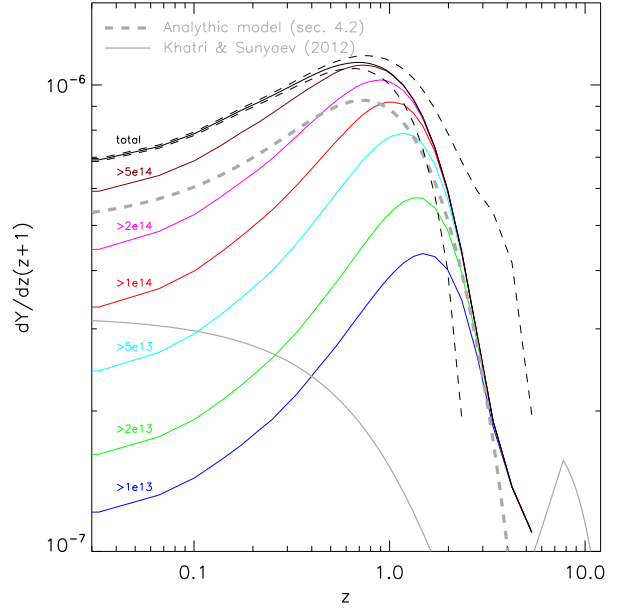

Figure 7. How the mean Compton Y builds up over time, $d\bar{Y}/d\ln(1 + z)$. All redshifts below $z \approx 1.5$ contribute to the total signal (black solid line) almost equally, to within 30%. The coloured lines show $d\bar{Y}/d\ln(1+z)$ with high-mass halos (whose virial masses are indicated by the numbers in units of $M_\odot/h$) removed from the simulation. Half of the signal at $z = 0$ comes from clusters with $M > 10^{14}\ M_\odot/h$, whereas at $z \approx 1$ the bulk of the signal comes from lower-mass halos. The dashed lines show the scatter due to kSZ at 150GHz. The bulk of kSZ comes from high redshift and non-collapsed regions. The gray solid line show approximate estimates of tSZ from the epoch of reionisation as well as from the intergalactic medium (IGM) at lower redshift taken from Khatri & Sunyaev (2012). The gray dashed line shows the analytical model for the contributions from halos.

area in the sky, we produce maps of the full simulation at each redshift. This allows us to compute $d\bar{Y}/dz$ at every snap shot with the same precision given by the comoving box size of our simulation, which is slightly more than 2 Gpc^3.

Figure 7 shows $d\bar{Y}/d\ln(1 + z)$ as a function of z, i.e., the time evolution of the contribution per logarithmic redshift interval to the overall signal. We find that all redshifts below $z \approx 1.5$ contribute almost equally to within 30%. To study which masses contribute, we also show $d\bar{Y}/d\ln(1 + z)$ with high-mass halos above a certain mass threshold removed from the simulation. At $z = 0$, half of the signal comes from $M > 10^{14}\ M_\odot/h$, whereas at $z \approx 1$ smaller halos dominate. We find that, even at $z = 0$, there is more than 10% of $d\bar{Y}/d\ln(1 + z)$ coming from outside of resolved objects, e.g., the diffuse baryon component. This fraction increases at higher redshifts and reaches almost 30% at $z \approx 1$.

We also show an order-of-magnitude comparison (gray solid line) by Khatri & Sunyaev (2012) of the contribution from the epoch of reionisation and from low redshift WHIM. The first one is based on the reionisation optical depth inferred from CMB observations by WMAP whereas the later one is based on the simulations of Cen & Ostriker (1999) and assumes that the temperature of IGM is 10^4 K at $z > 3$ and $10^6/(1 + z)^{3.3}$ K at $z < 3$ and does not include the contribution of massive clusters of galaxies. While these rough estimates cannot be compared quantitatively with the simulation results, it demonstrates that these contributions are much
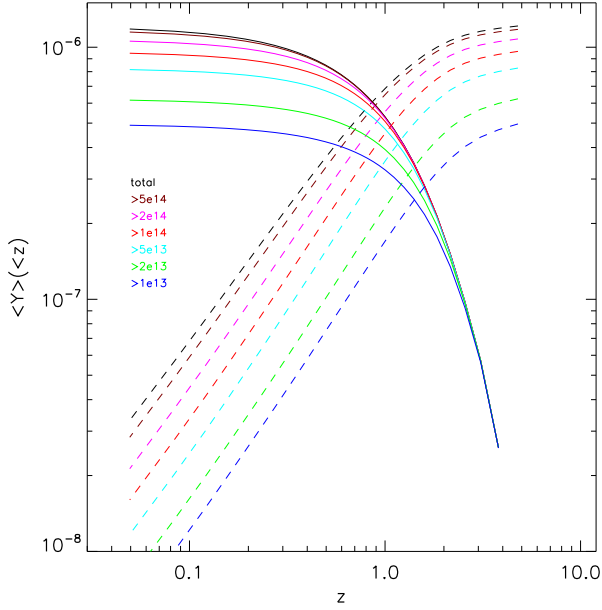
Figure 8. Same as figure 7, but for the cumulative signals. The solid lines show $\bar{Y}(> z) = \int_z^{5.2} dz' \ d\bar{Y}/dz'$, while the dashed lines show $\bar{Y}(< z) = \int_0^z dz' \ d\bar{Y}/dz'$.

Figure 9. PDFs of $dY/d\ln(1 + z)$ at $z = 0$ (black), 0.5 (blue), 1 (red), and 2 (green).

smaller than those from hot gas in galaxy clusters in the simulation.

The dashed gray line shows the analytical model of the contributions of halos computed with the mass function of Tinker et al. (2010) and the Planck pressure profile with the mass bias of 1.2. The analytical model does a reasonable job describing the simulation result, although it is systematically lower than the simulation by 20% at $z \lesssim 1$. See section 4.2 for more detailed discussion on the analytical model.

The dashed black lines show the scatter due to kSZ at 150 GHz. The kSZ is most prominent at high redshift and starts to contribute even earlier than tSZ does.

In figure 8, we show the evolution of the cumulative mean Compton Y. The solid lines show $\bar{Y}(> z) = \int_z^{5.2} dz' \ d\bar{Y}/dz$, while the dashed lines show $\bar{Y}(< z) = \int_0^z dz' \ d\bar{Y}/dz$. The latter clearly shows that the mean Compton Y receives significant contributions up to $z \approx 2$. We find that cluster-size halos with $M > 10^{14} \ M_\odot/h$ contribute only 20% of the total signal, and nearly half of the signal, $\bar{Y} = 5 \times 10^{-7}$, comes from $M < 10^{13} \ M_\odot/h$ (which can be detected by stacking; Planck Collaboration et al. 2013d; Gralla et al. 2014; Greco et al. 2015) and the diffuse baryons outside halos.

4.2 Analytical model

The analytical model for the mean Compton Y is given analogously to Eq. 7 (Barbosa et al. 1996)

$$\bar{Y} = g(x) \int_0^5 dz \frac{dV}{dz} \int_{M_{\min}}^{M_{\max}} d\ln M \frac{dn(M, z)}{d\ln M} \tilde{y}_0(M, z), \quad (12)$$

where $\tilde{y}_0$ is Eq. 9 with $l = 0$. However, as the mean Compton Y receives significant contributions from lower mass halos compared to the power spectrum, we use $M_{\min} = 5 \times 10^{10} \ M_\odot/h$. As our goal in this section is to confirm the result of the previous section,
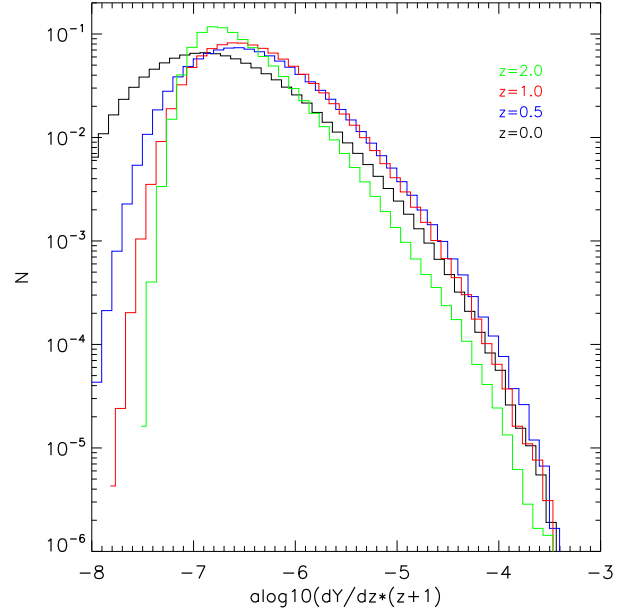
we use the cosmological parameters of the Magneticum Pathfinder simulation. All the other details of the calculation are the same as in section 3.3.2.

We find $\bar{Y} = (0.78, 0.61, 0.99) \times 10^{-6}$ for the mass functions of Bocquet et al. (2015), Tinker et al. (2008), and Tinker et al. (2010), respectively. The mean Compton Y receives significant contributions from low-mass halos for which these mass functions differ significantly. In particular, the former two fitting functions do not satisfy the normalisation constraint on the mass function, $\int_0^\infty dM_{200m} \ dn/d\ln M_{200m} = \bar{\rho}$. A reasonable agreement between the results from the simulation and the analytical model with the mass function of Tinker et al. (2010), which does satisfy the normalisation constraint, is encouraging; however, more study on a low-mass end of the mass function is necessary. The remaining difference of order 20% relative to the simulation is due to the Planck pressure profile with the mass bias of 1.2 being slightly lower than the pressure profiles in the simulation in lower mass halos ($M \lesssim 10^{14} \ M_\odot$). The same trend can be seen in the tSZ power spectrum at $l \gtrsim 3000$ shown in figure 6. For example, we find $\bar{Y} = (1.07, 1.16) \times 10^{-6}$ with the mass biases of 1.15 and 1.1, respectively. However, the mass bias of 1.1 would yield too large a tSZ power spectrum at low multipoles, $l \lesssim 1000$, to agree with the simulation.

Using the Planck 2015 parameters, the mass function of Tinker et al. (2010) and the mass bias of 1.2, we find $\bar{Y} = 1.32 \times 10^{-6}$. Using this to scale the simulation result, we find $\bar{Y} = 1.57 \times 10^{-6}$.

Recently, Hill et al. (2015) use the analytical model with the mass function of Tinker et al. (2010) and the pressure profile of Battaglia et al. (2012) to obtain $\bar{Y} = 1.58 \times 10^{-6}$ for the WMAP9 parameters with $\sigma_8 = 0.817$ and $\Omega_m = 0.282$ (Hinshaw et al. 2013). One minor detail on the calculation is different: while they integrate the pressure profile out to twice the virial radius, we integrate out to $6r_{500}$. Changing the upper integration boundary from $x_{\max} = 6$ to $2r_{\rm vir}/r_{500}$ in Eq. 9, we find $\bar{Y} = 1.04 \times 10^{-6}$ for the Planck pressure profile with the mass bias of 1.2 and the
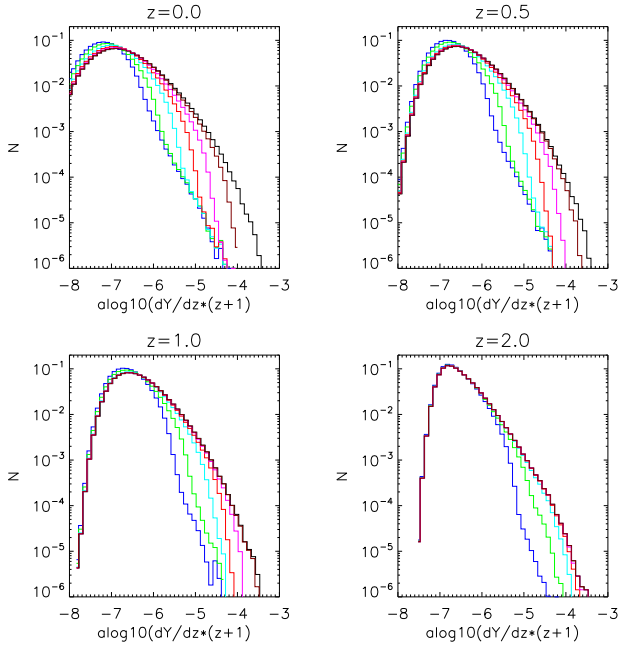
Figure 10. PDFs of $dY/d\ln(1 + z)$ at $z = 0$ (top left), 0.5 (top right), 1 (bottom left), and 2 (bottom right). In each panel, we show PDFs with high-mass halos above a certain mass threshold removed from the simulation. The colours indicate the same mass thresholds as shown in figure 7.

same WMAP9 parameters. This value is significantly lower than their value. We find that this is due to the difference in the pressure profiles; while the pressure profiles of the Magneticum Pathfinder simulation, the Planck pressure profile with the mass bias of 1.2, and the profile of Battaglia et al. (2012) agree in the high-mass end, $M_{500} \gtrsim 2 \times 10^{14} \ M_\odot/h$ (Planck Collaboration et al. 2013a), the latter profile gives significantly larger pressure than the Planck profile in lower masses that dominate in $\bar{Y}$.

These discrepancies need to be understood before we obtain an accurate estimate of the expected level of $\bar{Y}$. Nevertheless, the original conclusion from the previous generation of cosmological hydrodynamical simulations (Refregier et al. 2000; da Silva et al. 2000; Seljak et al. 2001; Zhang et al. 2004b) seems robust: the expected $\bar{Y}$ from the large-scale structure is of order 10^{-6} and is only one order of magnitude lower than the FIRAS bound. It is also encouraging that none of these estimates exceed the new Planck bound on the fluctuating part of the mean Y parameter, $\bar{Y} < 2.2 \times 10^{-6}$ (Khatri & Sunyaev 2015).

4.3 Buildup of the Compton Y PDF

Finally, we study contributions from different redshifts to the build up of the PDF of the Compton Y signal. Figure 9 shows the PDF of $dY/d\ln(1+z)$ at four different redshifts. Although these PDFs look at first glance similar to the one of the full light-cone (as shown in figure 5), the tail does not follow a simple power law. In general, with decreasing redshift, the PDF becomes broader and less sharply peaked, especially when compared to the PDF at $z = 2$.

In figure 10, we show PDFs with high-mass halos above a certain mass threshold removed from the simulation. At any given time, the tail is dominated by the most massive halos of that time.

5   CONCLUSIONS

The Magneticum Pathfinder simulations, state-of-the-art cosmological and hydrodynamical simulations, follow in detail the thermal and chemical evolution of the ICM as well as the evolution of super-massive black holes and their associated feedback processes. These simulations reproduce the average ICM pressure profiles measured by Planck (Planck Collaboration et al. 2013a) and SPT (McDonald et al. 2014). At the same time, the stellar mass functions of galaxies and the luminosity functions of the AGN population agree well with observations (Hirschmann et al. 2014). The improved numerical methods and increased computing power available today have enabled these simulations to follow a large enough cosmological volume to construct realistic light-cone maps, which can be compared with observations in detail.

In this paper, we have computed the tSZ and kSZ effects toward the counterpart of the Coma cluster in the local universe simulation, and statistics of the SZ effects from the light-cone maps, including the one-point PDF and power spectrum of tSZ and kSZ, and the mean Compton Y parameter. We have then compared these predictions on tSZ with the Planck, SPT, and ACT data. Our findings are summarised as follows:

• The tSZ radial profile of Coma in the local universe simulation embedded in the background from the deep light-cone agrees well with that in the Planck data.

• The local universe simulation predicts that the halo of Coma is moving away from us at ≈ 400 km/s with respect to the CMB rest frame, thus yielding a negative kSZ within the central region of Coma. The magnitude of kSZ is ten percent of tSZ at 150 GHz. On the other hand, because Coma is a merging system, we find a significant relative motion of the core (even increasing the negative signal in the center) and a significant positive kSZ in the outskirt, which comes from a infalling sub-structure moving toward us. This makes a positive kSZ contribution to tSZ at 150 GHz at distances beyond 1 Mpc from the center of Coma.

• The predicted one-point PDF of the Compton Y agrees with that measured by Planck, once the simulations are smoothed to the resolution of Planck's Y map (10 arcmin). Given the much smaller beam size, we expect that ACT- and SPT-like instruments will see almost the full PDF that is resolved by our simulations. The tail of the full PDF follows a power-law with an index of -3.2.

• The tSZ power spectrum measured from the simulation agrees with that of the Planck data at all multipoles up to $l \approx 1000$, once the power spectrum is rescaled to Planck 2015's "TT+lowP+lensing" cosmological parameters with $\Omega_m = 0.308$ and $\sigma_8 = 0.8149$ (Planck Collaboration et al. 2015a). We have confirmed and understood this result using the analytical model.

• Consistent with the previous work, we continue to find the predicted tSZ power spectrum at $l = 3000$ that is significantly higher than that estimated by ACT and SPT. Whether this poses a challenge to theory is unclear, but our prediction is still well below the firm upper bound on tSZ given by the SPT data points with the primary CMB subtracted.

• The simulation predicts the mean Compton Y value of 1.18×10^{-6} for $\Omega_m = 0.272$ and $\sigma_8 = 0.809$. When the contributions from halos above a virial mass of $10^{13} \ M_\odot/h$ are removed, we find $\bar{Y} = 5 \times 10^{-7}$; thus, nearly half of the signal comes from such low-mass halos and diffuse gas outside halos. This remaining signal would pose a challenge to detecting the primordial y-distortions.

• Using the analytical model, we scale the Compton Y value from the simulation to the Planck 2015 parameters with $\Omega_m = 0.308$ and $\sigma_8 = 0.8149$, finding $\bar{Y} = 1.57 \times 10^{-6}$. This is still

lower than, but not far away from, the new Planck bound, $\bar{Y} < 2.2 \times 10^{-6}$ (Khatri & Sunyaev 2015).

- The one-point PDF and the power spectrum of kSZ from our simulations agree broadly with the previous work. While our box size is large, the contribution to kSZ is still dominated by the largest modes within the box and originates mainly from high redshifts. Therefore, unlike for tSZ, we have not yet obtained a reliable, converged result on kSZ on large scales, $l \lesssim 1000$. Simulations following even large cosmological volumes are needed.

In short, the main conclusion from our study is that all the properties of tSZ found in the Magneticum Pathfinder simulation and the local universe simulation agree well with the Planck data. This includes the tSZ power spectrum, which was previously found to be in tension with the Planck 2013 parameters (Planck Collaboration et al. 2014b; McCarthy et al. 2014). Now, the tSZ power spectrum calculated for the Planck 2015 parameters including CMB lensing information agrees with the measurement at all multipoles up to $l \approx 1000$.

REFERENCES

Arnaud, M., Pratt, G. W., Piffaretti, R., Böhringer, H., Croston, J. H., & Pointecouteau, E. 2010a, A&A, 517, A92

—. 2010b, A&A, 517, A92

Barbosa, D., Bartlett, J. G., Blanchard, A., & Oukbir, J. 1996, A&A, 314, 13

Battaglia, N., Bond, J. R., Pfrommer, C., & Sievers, J. L. 2012, ApJ, 758, 75

Battaglia, N., Bond, J. R., Pfrommer, C., Sievers, J. L., & Sijacki, D. 2010, ApJ, 725, 91

Bocquet, S., Saro, A., Dolag, K., & Mohr, J. J. 2015, ArXiv e-prints

Bondi, H. 1952, MNRAS, 112, 195

Bondi, H. & Hoyle, F. 1944, MNRAS, 104, 273

Cen, R. & Ostriker, J. P. 1999, ApJ, 514, 1

Chabrier, G. 2003, PASP, 115, 763

da Silva, A. C., Barbosa, D., Liddle, A. R., & Thomas, P. A. 2000, MNRAS, 317, 37

—. 2001a, MNRAS, 326, 155

da Silva, A. C., Kay, S. T., Liddle, A. R., Thomas, P. A., Pearce, F. R., & Barbosa, D. 2001b, ApJ, 561, L15

Di Matteo, T., Springel, V., & Hernquist, L. 2005, Nature, 433, 604

Dolag, K., Hansen, F. K., Roncarelli, M., & Moscardini, L. 2005a, MNRAS, 363, 29

Dolag, K., Jubelgas, M., Springel, V., Borgani, S., & Rasia, E. 2004, ApJ, 606, L97

Dolag, K. & Sunyaev, R. 2013, MNRAS, 432, 1600

Dolag, K., Vazza, F., Brunetti, G., & Tormen, G. 2005b, MNRAS, 364, 753

Duffy, A. R., Schaye, J., Kay, S. T., & Dalla Vecchia, C. 2008, MNRAS, 390, L64

Fabjan, D., Borgani, S., Tornatore, L., Saro, A., Murante, G., & Dolag, K. 2010, MNRAS, 401, 1670

Ferland, G. J., Korista, K. T., Verner, D. A., Ferguson, J. W., Kingdon, J. B., & Verner, E. M. 1998, PASP, 110, 761

Fisher, K. B., Davis, M., Strauss, M. A., Yahil, A., & Huchra, J. P. 1994, MNRAS, 267, 927

Fisher, K. B., Huchra, J. P., Strauss, M. A., Davis, M., Yahil, A., & Schlegel, D. 1995, ApJS, 100, 69

Fixsen, D. J., Cheng, E. S., Gales, J. M., Mather, J. C., Shafer, R. A., & Wright, E. L. 1996, ApJ, 473, 576

George, E. M., Reichardt, C. L., Aird, K. A., Benson, B. A., Bleem, L. E., Carlstrom, J. E., Chang, C. L., Cho, H.-M., Crawford, T. M., Crites, A. T., de Haan, T., Dobbs, M. A., Dudley, J., Halverson, N. W., Harrington, N. L., Holder, G. P., Holzapfel, W. L., Hou, Z., Hrubes, J. D., Keisler, R., Knox, L., Lee, A. T., Leitch, E. M., Lueker, M., Luong-Van, D., McMahon, J. J., Mehl, J., Meyer, S. S., Millea, M., Mocanu, L. M., Mohr, J. J., Montroy, T. E., Padin, S., Plagge, T., Pryke, C., Ruhl, J. E., Schaffer, K. K., Shaw, L., Shirokoff, E., Spieler, H. G., Staniszewski, Z., Stark, A. A., Story, K. T., van Engelen, A., Vanderlinde, K., Vieira, J. D., Williamson, R., & Zahn, O. 2015, ApJ, 799, 177

Górski, K. M., Hivon, E., & Wandelt, B. D. 1998, 'Analysis Issues for Large CMB Data Sets', 1998, eds A. J. Banday, R. K. Sheth and L. Da Costa, ESO, Printpartners Ipskamp, NL, pp.37-42 (astro-ph/9812350); Healpix HOMEPAGE: http://www.eso.org/science/healpix/

Gralla, M. B., Crichton, D., Marriage, T. A., Mo, W., Aguirre, P., Addison, G. E., Asboth, V., Battaglia, N., Bock, J., Bond, J. R., Devlin, M. J., Dünner, R., Hajian, A., Halpern, M., Hilton, M., Hincks, A. D., Hlozek, R. A., Huffenberger, K. M., Hughes, J. P., Ivison, R. J., Kosowsky, A., Lin, Y.-T., Marsden, D., Menanteau, F., Moodley, K., Morales, G., Niemack, M. D., Oliver, S., Page, L. A., Partridge, B., Reese, E. D., Rojas, F., Sehgal, N., Sievers, J., Sifón, C., Spergel, D. N., Staggs, S. T., Switzer, E. R., Viero, M. P., Wollack, E. J., & Zemcov, M. B. 2014, MNRAS, 445, 460

Greco, J. P., Hill, J. C., Spergel, D. N., & Battaglia, N. 2015, ApJ, 808, 151

Haardt, F. & Madau, P. 2001, in Clusters of Galaxies and the High Redshift Universe Observed in X-rays, ed. D. M. Neumann & J. T. V. Tran

Hand, N., Addison, G. E., Aubourg, E., Battaglia, N., Battistelli, E. S., Bizyaev, D., Bond, J. R., Brewington, H., Brinkmann, J., Brown, B. R., Das, S., Dawson, K. S., Devlin, M. J., Dunkley, J., & Dunner, R. e. a. 2012, Physical Review Letters, 109, 041101

Hansen, F. K., Branchini, E., Mazzotta, P., Cabella, P., & Dolag, K. 2005, MNRAS, 361, 753

Hernández-Monteagudo, C. & Ho, S. 2009, MNRAS, 398, 790

Hill, J. C., Battaglia, N., Chluba, J., Ferraro, S., Schaan, E., & Spergel, D. N. 2015, ArXiv e-prints

Hill, J. C., Sherwin, B. D., Smith, K. M., Addison, G. E., Battaglia, N., Battistelli, E. S., Bond, J. R., Calabrese, E., Devlin, M. J., Dunkley, J., Dunner, R., Essinger-Hileman, T., Gralla, M. B., Hajian, A., Hasselfield, M., Hincks, A. D., Hlozek, R., Hughes, J. P., Kosowsky, A., Louis, T., Marsden, D., Moodley, K., Niemack, M. D., Page, L. A., Partridge, B., Schmitt, B., Sehgal, N., Sievers, J. L., Spergel, D. N., Staggs, S. T., Swetz, D. S.,

Thornton, R., Trac, H., & Wollack, E. J. 2014, ArXiv e-prints

Hinshaw, G., Larson, D., Komatsu, E., Spergel, D. N., Bennett, C. L., Dunkley, J., Nolta, M. R., Halpern, M., Hill, R. S., Odegard, N., Page, L., Smith, K. M., Weiland, J. L., Gold, B., Jarosik, N., Kogut, A., Limon, M., Meyer, S. S., Tucker, G. S., Wollack, E., & Wright, E. L. 2013, ApJS, 208, 19

Hirschmann, M., Dolag, K., Saro, A., Bachmann, L., Borgani, S., & Burkert, A. 2014, MNRAS, 442, 2304

Hoffman, Y. & Ribak, E. 1991, ApJ, 380, L5

Hoyle, F. & Lyttleton, R. A. 1939, Proceedings of the Cambridge Philosophical Society, 35, 405

Khatri, R. 2015, astro-ph/150500778

Khatri, R. & Sunyaev, R. A. 2012, JCAP, 9, 16

—. 2015, JCAP, 8, 13

Kogut, A., Chuss, D. T., Dotson, J., Dwek, E., Fixsen, D. J., Halpern, M., Hinshaw, G. F., Meyer, S., Moseley, S. H., Seiffert, M. D., Spergel, D. N., & Wollack, E. J. 2014, 9143, 1

Kolatt, T., Dekel, A., Ganon, G., & Willick, J. A. 1996, ApJ, 458, 419

Komatsu, E. & Kitayama, T. 1999, ApJ, 526, L1

Komatsu, E. & Seljak, U. 2001, MNRAS, 327, 1353

—. 2002, MNRAS, 336, 1256

Komatsu, E., Smith, K. M., Dunkley, J., Bennett, C. L., Gold, B., Hinshaw, G., Jarosik, N., Larson, D., Nolta, M. R., Page, L., Spergel, D. N., & Halpern, M. 2011, ApJS, 192, 18

Lewis, A., Challinor, A., & Lasenby, A. 2000, ApJ, 538, 473

Li, M., Angulo, R. E., White, S. D. M., & Jasche, J. 2014, MNRAS, 443, 2311

Mathis, H., Lemson, G., Springel, V., Kauffmann, G., White, S. D. M., Eldar, A., & Dekel, A. 2002, MNRAS, 333, 739

McCarthy, I. G., Le Brun, A. M. C., Schaye, J., & Holder, G. P. 2014, MNRAS, 440, 3645

McDonald, M., Benson, B. A., Vikhlinin, A., Aird, K. A., Allen, S. W., Bautz, M., Bayliss, M., Bleem, L. E., Bocquet, S., Brodwin, M., Carlstrom, J. E., Chang, C. L., Cho, H. M., Clocchiatti, A., Crawford, T. M., Crites, A. T., de Haan, T., Dobbs, M. A., Foley, R. J., Forman, W. R., George, E. M., Gladders, M. D., Gonzalez, A. H., Halverson, N. W., Hlavacek-Larrondo, J., Holder, G. P., Holzapfel, W. L., Hrubes, J. D., Jones, C., Keisler, R., Knox, L., Lee, A. T., Leitch, E. M., Liu, J., Lueker, M., Luong-Van, D., Mantz, A., Marrone, D. P., McMahon, J. J., Meyer, S. S., Miller, E. D., Mocanu, L., Mohr, J. J., Murray, S. S., Padin, S., Pryke, C., Reichardt, C. L., Rest, A., Ruhl, J. E., Saliwanchik, B. R., Saro, A., Sayre, J. T., Schaffer, K. K., Shirokoff, E., Spieler, H. G., Stalder, B., Stanford, S. A., Staniszewski, Z., Stark, A. A., Story, K. T., Stubbs, C. W., Vanderlinde, K., Vieira, J. D., Williamson, R., Zahn, O., & Zenteno, A. 2014, ApJ, 794, 67

Munshi, D., Joudaki, S., Smidt, J., Coles, P., & Kay, S. T. 2013, MNRAS, 429, 1564

Nagai, D., Kravtsov, A. V., & Vikhlinin, A. 2007, ApJ, 668, 1

Navarro, J. F., Frenk, C. S., & White, S. D. M. 1996, ApJ, 462, 563

—. 1997, ApJ, 490, 493

Padovani, P. & Matteucci, F. 1993, ApJ, 416, 26

Park, H., Komatsu, E., Shapiro, P. R., Koda, J., & Mao, Y. 2015, ArXiv e-prints

Park, H., Shapiro, P. R., Komatsu, E., Iliev, I. T., Ahn, K., & Mellema, G. 2013, ApJ, 769, 93

Persi, F. M., Spergel, D. N., Cen, R., & Ostriker, J. P. 1995, ApJ, 442, 1

Planck Collaboration, Ade, P. A. R., Aghanim, N., Armitage-

Caplan, C., Arnaud, M., Ashdown, M., Atrio-Barandela, F., Aumont, J., Baccigalupi, C., Banday, A. J., & et al. 2014a, A&A, 571, A16

—. 2014b, A&A, 571, A21

Planck Collaboration, Ade, P. A. R., Aghanim, N., Arnaud, M., Ashdown, M., Atrio-Barandela, F., Aumont, J., Baccigalupi, C., Balbi, A., Banday, A. J., & et al. 2013a, A&A, 550, A131

—. 2013b, A&A, 550, A131

—. 2013c, A&A, 554, A140

—. 2013d, A&A, 557, A52

Planck Collaboration, Ade, P. A. R., Aghanim, N., Arnaud, M., Ashdown, M., Aumont, J., Baccigalupi, C., Banday, A. J., Barreiro, R. B., Bartlett, J. G., & et al. 2015a, ArXiv 1502.01589

—. 2015b, ArXiv e-prints

Planck Collaboration, Aghanim, N., Arnaud, M., Ashdown, M., Aumont, J., Baccigalupi, C., Banday, A. J., Barreiro, R. B., Bartlett, J. G., Bartolo, N., & et al. 2015c, ArXiv 1502.01596

Ramos-Ceja, M. E., Basu, K., Pacaud, F., & Bertoldi, F. 2014, ArXiv e-prints

Refregier, A., Komatsu, E., Spergel, D. N., & Pen, U.-L. 2000, Phys. Rev. D, 61, 123001

Refregier, A. & Teyssier, R. 2002, Phys. Rev. D, 66, 043002

Reichardt, C. L., Shaw, L., Zahn, O., Aird, K. A., Benson, B. A., Bleem, L. E., Carlstrom, J. E., Chang, C. L., Cho, H. M., Crawford, T. M., Crites, A. T., de Haan, T., Dobbs, M. A., Dudley, J., George, E. M., Halverson, N. W., Holder, G. P., Holzapfel, W. L., Hoover, S., Hou, Z., Hrubes, J. D., Joy, M., Keisler, R., Knox, L., Lee, A. T., Leitch, E. M., Lueker, M., Luong-Van, D., McMahon, J. J., Mehl, J., Meyer, S. S., Millea, M., Mohr, J. J., Montroy, T. E., Natoli, T., Padin, S., Plagge, T., Pryke, C., Ruhl, J. E., Schaffer, K. K., Shirokoff, E., Spieler, H. G., Staniszewski, Z., Stark, A. A., Story, K., van Engelen, A., Vanderlinde, K., Vieira, J. D., & Williamson, R. 2012, ApJ, 755, 70

Roncarelli, M., Moscardini, L., Borgani, S., & Dolag, K. 2007, MNRAS, 378, 1259

Rubiño-Martín, J. A. & Sunyaev, R. A. 2003, MNRAS, 344, 1155

Seljak, U., Burwell, J., & Pen, U.-L. 2001, Phys. Rev. D, 63, 063001

Shakura, N. I. & Sunyaev, R. A. 1973, A&A, 24, 337

Shaw, L. D., Nagai, D., Bhattacharya, S., & Lau, E. T. 2010, ApJ, 725, 1452

Shaw, L. D., Rudd, D. H., & Nagai, D. 2012, ApJ, 756, 15

Shi, X. & Komatsu, E. 2014, MNRAS, 442, 521

Sievers, J. L., Hlozek, R. A., Nolta, M. R., Acquaviva, V., Addison, G. E., Ade, P. A. R., Aguirre, P., Amiri, M., Appel, J. W., Barrientos, L. F., Battistelli, E. S., Battaglia, N., Bond, J. R., Brown, B., Burger, B., Calabrese, E., Chervenak, J., Crichton, D., Das, S., Devlin, M. J., Dicker, S. R., Bertrand Doriese, W., Dunkley, J., Dünner, R., Essinger-Hileman, T., Faber, D., Fisher, R. P., Fowler, J. W., Gallardo, P., Gordon, M. S., Gralla, M. B., Hajian, A., Halpern, M., Hasselfield, M., Hernández-Monteagudo, C., Hill, J. C., Hilton, G. C., Hilton, M., Hincks, A. D., Holtz, D., Huffenberger, K. M., Hughes, D. H., Hughes, J. P., Infante, L., Irwin, K. D., Jacobson, D. R., Johnstone, B., Baptiste Juin, J., Kaul, M., Klein, J., Kosowsky, A., Lau, J. M., Limon, M., Lin, Y.-T., Louis, T., Lupton, R. H., Marriage, T. A., Marsden, D., Martocci, K., Mauskopf, P., McLaren, M., Menanteau, F., Moodley, K., Moseley, H., Netterfield, C. B., Niemack, M. D., Page, L. A., Page, W. A., Parker, L., Partridge, B., Plimpton, R., Quintana, H., Reese, E. D., Reid, B., Rojas, F., Sehgal, N., Sherwin, B. D., Schmitt, B. L., Spergel, D. N., Staggs, S. T., Stryzak, O., Swetz, D. S., Switzer, E. R., Thornton, R., Trac,

H., Tucker, C., Uehara, M., Visnjic, K., Warne, R., Wilson, G., Wollack, E., Zhao, Y., & Zunckel, C. 2013, JCAP, 10, 60

Sijacki, D., Springel, V., Di Matteo, T., & Hernquist, L. 2007, MNRAS, 380, 877

Spergel, D. N., Flauger, R., & Hložek, R. 2015, Phys. Rev. D, 91, 023518

Spitzer, L. 1962, Physics of Fully Ionized Gases

Springel, V. 2005, MNRAS, 364, 1105

Springel, V., Di Matteo, T., & Hernquist, L. 2005, MNRAS, 361, 776

Springel, V. & Hernquist, L. 2002, MNRAS, 333, 649

—. 2003, MNRAS, 339, 289

Springel, V., White, M., & Hernquist, L. 2001, ApJ, 549, 681

Sunyaev, R. A. & Zeldovich, Y. B. 1970a, Ap&SS, 7, 3

—. 1970b, Comments on Astrophysics and Space Physics, 2, 66

—. 1972, Comments on Astrophysics and Space Physics, 4, 173

—. 1980a, ARAA, 18, 537

—. 1980b, MNRAS, 190, 413

Thielemann, F.-K., Argast, D., Brachwitz, F., Hix, W. R., Höflich, P., Liebendörfer, M., Martinez-Pinedo, G., Mezzacappa, A., Panov, I., & Rauscher, T. 2003, Nuclear Physics A, 718, 139

Tinker, J., Kravtsov, A. V., Klypin, A., Abazajian, K., Warren, M., Yepes, G., Gottlöber, S., & Holz, D. E. 2008, ApJ, 688, 709

Tinker, J. L., Robertson, B. E., Kravtsov, A. V., Klypin, A., Warren, M. S., Yepes, G., & Gottlöber, S. 2010, ApJ, 724, 878

Tornatore, L., Borgani, S., Dolag, K., & Matteucci, F. 2007, MNRAS, 382, 1050

van den Hoek, L. B. & Groenewegen, M. A. T. 1997, A&AS, 123, 305

White, M., Hernquist, L., & Springel, V. 2002, ApJ, 579, 16

Wiersma, R. P. C., Schaye, J., & Smith, B. D. 2009, MNRAS, 393, 99

Woosley, S. E. & Weaver, T. A. 1995, ApJS, 101, 181

Yoshida, N., Sheth, R. K., & Diaferio, A. 2001, MNRAS, 328, 669

Zahn, O., Reichardt, C. L., Shaw, L., Lidz, A., Aird, K. A., Benson, B. A., Bleem, L. E., Carlstrom, J. E., Chang, C. L., Cho, H. M., Crawford, T. M., Crites, A. T., de Haan, T., Dobbs, M. A., Doré, O., Dudley, J., George, E. M., Halverson, N. W., Holder, G. P., Holzapfel, W. L., Hoover, S., Hou, Z., Hrubes, J. D., Joy, M., Keisler, R., Knox, L., Lee, A. T., Leitch, E. M., Lueker, M., Luong-Van, D., McMahon, J. J., Mehl, J., Meyer, S. S., Millea, M., Mohr, J. J., Montroy, T. E., Natoli, T., Padin, S., Plagge, T., Pryke, C., Ruhl, J. E., Schaffer, K. K., Shirokoff, E., Spieler, H. G., Staniszewski, Z., Stark, A. A., Story, K., van Engelen, A., Vanderlinde, K., Vieira, J. D., & Williamson, R. 2012, ApJ, 756, 65

Zeldovich, Y. B. & Sunyaev, R. A. 1969, Ap&SS, 4, 301

Zhang, P., Pen, U.-L., & Trac, H. 2004a, MNRAS, 347, 1224

—. 2004b, MNRAS, 355, 451

Zhang, P., Pen, U.-L., & Wang, B. 2002, ApJ, 577, 555

ZuHone, J. A., Markevitch, M., & Johnson, R. E. 2010, ApJ, 717, 908